ARTICLE

Check for updates

Journal of
Sensor Science and Technology

The Korean Sensors Society

Experimental Assessment of a Three-Axis Magnetic Induction Sensor for Magnetic Field Communication

Jang-Yeol Kim[1,+], In-Kui Cho[1], Hyun Joon Lee[1], Jung Hoon Oh[1], Kye-Seok Yoon[1], and Jae-Ho Lee[2]

[1]*Radio Research Division, Electronics and Telecommunications Research Institute, 218 Gajeong-ro, Yuseong-gu, Daejeon, 31420, Republic of Korea*
[2]*Department of Electronic Engineering, Kunsan National University, 558 Daehak-ro, Jellabuk-do, 54150, Republic of Korea*

Cite This: *J. Sens. Sci. Technol. Vol. 34, No. 4 (2025) 251-260*

https://doi.org/10.46670/JSST.2025.34.4.251

ABSTRACT: A novel three-axis magnetic induction (MI) sensor is proposed as a receiving element for mid-to-long-range magnetic field communication in harsh environments, such as underwater and underground conditions. The sensor provides omni-directional reception of transmitted signals without requiring orientation information of the transmitter, effectively overcoming the directional limitations of single- or two-axis MI sensors. It achieves an equivalent magnetic noise spectral density (EMNSD) less than 0.5 pT/√Hz at 20 kHz, enabling the detection of weak magnetic fields for reliable communication. A communication test was conducted using quadrature phase-shift keying (QPSK) modulation scheme in a laboratory setting to evaluate its feasibility. Experimental results confirmed successful reception and demodulation of both textual and image data signals at 20 kHz, with a maximum data rate of 12 kbps achieved for text transmission.

KEYWORDS: *Three-axis magnetic sensor, Magnetic field communication, Harsh environment*

1. INTRODUCTION

Radio frequency (RF) sensors have emerged as a key technology in wireless sensor networks (WSNs) owing to their wide range of applications and increasing importance in various fields. Consequently, significant research has been conducted to improve the performance of RF sensors and expand their applicability to diverse environments [1-7]. Recently, research has increasingly focused on employing RF magnetic sensors for communication in harsh environments, such as underwater and underground environments, resulting in accelerated developments in this area [8-11,13-16].

Conventional electric field-based RF communication techniques often struggle to operate effectively under such conditions, primarily because of significant signal attenuation when electric fields propagate through heterogeneous media with different dielectric properties [12].

In contrast, magnetic fields are minimally affected by the permittivity and depend on the permeability of the surrounding media. This fundamental distinction provides a key advantage in minimizing the signal attenuation through heterogeneous media. Thus, magnetic-field-based RF communication techniques have emerged as promising alternatives because magnetic fields can penetrate heterogeneous media (e.g., air, water, and soil) with relatively low signal loss. Owing to these characteristics, magnetic-field-based RF communication is particularly well suited for underwater and underground communication, where conventional wireless systems suffer from limitations such as Doppler effects and multipath fading [13-16].

In near-field communication, conventional systems are constrained by limited transmission distances. As reported in [12], both Near Field Communication (NFC) and Radio Frequency Identification (RFID) wireless communication technologies operate at a common frequency of 13.56 MHz and are generally applicable to short-range communications within 10 cm. Furthermore, the communication range of RFID can be extended up to several meters depending on the frequency band. Therefore, conventional short-range wireless communication technologies are inherently limited in terms of transmission distance. To overcome this limitation, research-

[+]Corresponding author: jykim36@etri.re.kr
Received : Jun. 10, 2025, Accepted : Jun. 20, 2025

ers have increasingly explored magnetic induction (MI) sensors, which offer high magnetic field-to-voltage conversion ratio (MVCR) and the capability to detect ultra-weak magnetic fields at the pT/√Hz level, as potential receiving elements [8,9]. In addition, magnetic-field communication techniques utilizing magnetic sensors as receiving elements beyond MI sensors have been reported [7,10]. Ref. [7] presents research results on a magnetic field communication system employing an RF atomic magnetometer, whereas [10] reported a communication system utilizing a giant magneto-impedance sensor. MI sensors offer advantages over atomic magnetometers in terms of sensor implementation, system complexity, and bandwidth and are also favorable compared with giant magneto-impedance sensors in terms of sensor sensitivity and system simplicity. Owing to these advantages, along with the aforementioned merits of MI sensors, studies employing MI sensors as receiving elements have been increasingly reported.

In a previous study [8], the feasibility of magnetic field communication was experimentally demonstrated at the laboratory level using single-axis MI and single-axis differential MI (DMI) sensors. In addition, magnetic field communication link tests were conducted using a single-axis DMI sensor and a DMI sensor-based receiver in real-world environments, including a limestone underground mine [9] and a freshwater underwater environment [13]. The results confirmed the successful magnetic-field communication over a distance of 40 m, demonstrating that the communication distance can be extended to several tens of meters. In [15], a single-axis dual DMI sensor was presented as an enhanced MI sensor to extend the communication distance in harsh environments and investigate its potential as a receiving element for magnetic field communication.

In this paper, a novel three-axis MI sensor specifically designed for use as a receiving element in mid-to-long-range magnetic field communication, is proposed. The proposed three-axis MI sensor enables omni-directional signal reception without requiring prior information on the transmitter orientation. This capability facilitates reliable acquisition of transmitted signals and effectively overcomes the directional limitations inherent in conventional single- or two-axis MI sensors. A three-axis MI sensor was constructed by arranging and integrating identical single-axis MI sensors along the x-, y-, and z-axes. The single-axis MI sensors used in the three-axis MI sensor configuration were redesigned based on the single-axis MI sensor presented in [8] to improve performance. The improved single-axis MI sensor is characterized by altered design parameters, including the ferromagnetic core, wire diameter, and width of the pickup coil. These changes enhance sensor performance by increasing the MVCR and reducing the equivalent magnetic noise spectral density (EMNSD), both of which are crucial for extending the communication range and improving signal reliability in challenging environments. An experimental evaluation system was established to validate the feasibility of using a three-axis MI sensor as a receiving element for magnetic field communication. The system employed a Helmholtz coil as the transmitting antenna and adopted quadrature phase-shift keying (QPSK) modulation to achieve high data rates and improved noise resistance. This study demonstrated that the three-axis MI sensor exhibits potential as a robust and efficient magnetic field communication solution in harsh environments, such as underwater and underground scenarios.

2. DESIGN AND RESULTS

2.1 Sensor Design and Fabrication

The structure of the proposed three-axis MI sensor is shown in Fig. 1. The sensor was designed to function as a receiving element in a mid-to-long-range magnetic field communication

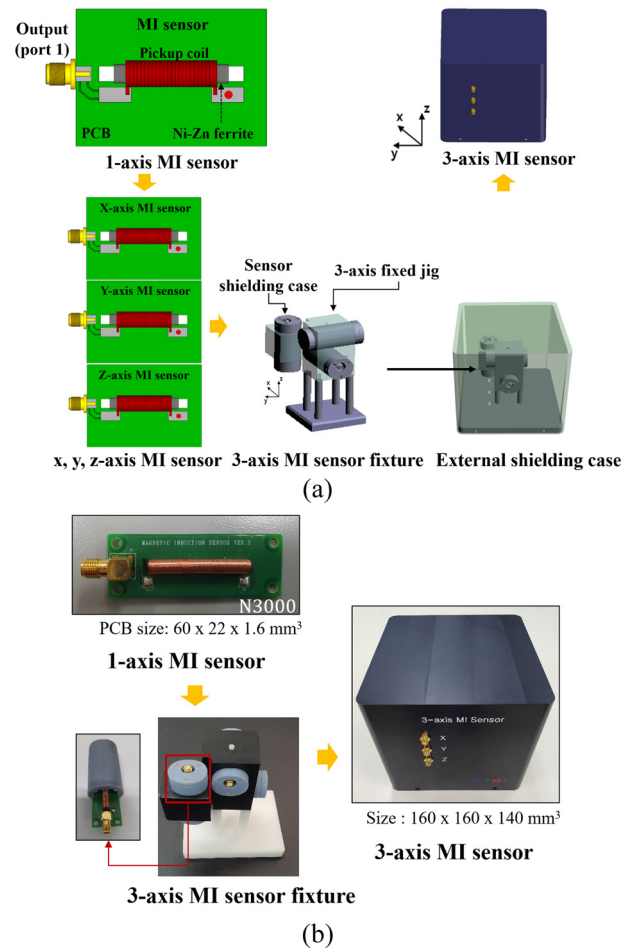

Fig. 1. Schematic and fabrication images of the proposed three-axis magnetic induction (MI) sensor: (a) schematic design. (b) fabricated sensor.

Table 1. Design parameters of the proposed three-axis MI sensor and a comparison with an existing MI sensor.

Parameter	MI sensor [8]	MI sensor (This work)
Core diameter	5 mm	5 mm
Core length	30 mm	35 mm
Core initial permeability	700	800
Number of cores	1	1
Diameter of the pickup coil wire	0.08 mm	0.04 mm
Number of turns of the pickup coil	3000	3000
Width of the pickup coil	28	33
Overall PCB size	55 × 22 × 1.6 mm^3	60 × 22 × 1.6 mm^3

system. Fig. 1 (a) shows the design of the three-axis MI sensor. To construct this three-axis MI sensor, we individually designed identical single-axis MI sensors based on a printed circuit board (PCB) for the x-, y-, and z-axes. This single-axis MI sensor was redesigned by modifying the design parameters of the conventional single-axis MI sensor reported in [8] to enhance the overall sensor performance, as detailed in Table 1. Additionally, single-axis MI sensors for the x-, y-, and z-axes were individually inserted into the shielding cases to provide physical protection. These shielding cases were mounted onto a three-axis fixed jig integrated into the fixture of the three-axis MI sensor. The MI sensors for the x-, y-, and z-axes, mounted on the three-axis MI sensor fixture, were arranged orthogonally at 90° with respect to each axis and integrated with an external shielding case. During integration, the output ports of the individual single-axis MI sensors were connected to the output port of the external shielding case via RF cables. This integration process completed the construction of the three-axis MI sensor.

Fig. 1 (b) shows the fabrication process and corresponding images of the three-axis MI sensor. A Ni-Zn ferrite with a relative permeability of 800 was selected as the soft magnetic material for the ferromagnetic core of the single-axis MI sensor. A single-axis MI sensor was fabricated on a PCB using FR4 material, which has a relative permittivity of 4.6. The overall dimensions of the sensor were 60 mm × 22 mm × 16 mm. The final three-axis MI sensor assembly measured 160 mm × 160 mm × 140 mm and was fabricated using acetal as the external shielding case, acrylonitrile-butadiene-styrene (ABS) as the sensor fixture, and resin as the sensor shielding case.

2.2 Experimental Results of Sensor

The performance of the proposed three-axis MI sensor was evaluated experimentally. For wireless power transmission, the lowest frequency band (19–21 kHz) recommended by the International Telecommunication Union Radiocommunication Sector, Study Group 1 (ITU- R/SG1), was employed for testing. The experiments were conducted at a center frequency of 20 kHz.

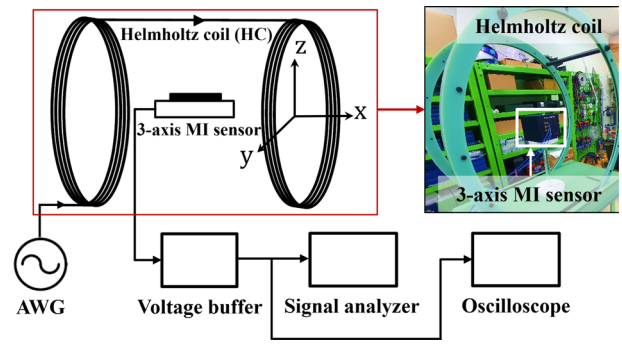

Fig. 2. Experimental setup and block diagram for the evaluation of the three-axis MI sensor.

Fig. 2 depicts the experimental setup for evaluating the proposed three-axis MI sensor. A Helmholtz coil with a diameter of 1 m was used as the transmitting antenna to generate a uniform magnetic field inside the coil. A uniform magnetic field was generated by an arbitrary waveform generator (AWG, Keysight 33500B) that supplied a signal to the Helmholtz coil. The three-axis MI sensor received the magnetic flux density generated inside the Helmholtz coil (where the sensor was placed) and produced a corresponding voltage output. The output voltage data from the sensor were collected using a signal analyzer (Rohde & Schwarz, FSV4) and an oscilloscope (Teledyne LeCroy, WaveSurfer 510).

The output voltage characteristics of the three-axis MI sensor were analyzed in both time and frequency domains. The results are shown in Fig. 3. When the AWG applied a 0.1 V_{pp} at 20 kHz to the Helmholtz coil, the resulting magnetic flux density converted to the x-axis direction inside the Helmholtz coil was Bx = 0.01 μT. The output voltage corresponding to the magnetic flux density received by the pickup coil of the x-axis MI sensor in the three-axis MI sensor is expressed as follows [8,17]:

$$v_{out} = -\frac{d\phi}{dt} = -\frac{NA\mu_0\mu_r dH}{dt} = -\frac{NAdB_x}{dt} \quad (1)$$

Considering the sinusoidal magnetic flux density $B_x = B_0 \sin \omega t = \mu_0\mu_r H_0 \sin(\omega t)$ was considered, the induced voltage of the pickup coil for the MI sensor is expressed as follows:

$$v_{out} = -NA\omega\mu_0\mu_r H_0 \cos(\omega t) \quad (2)$$

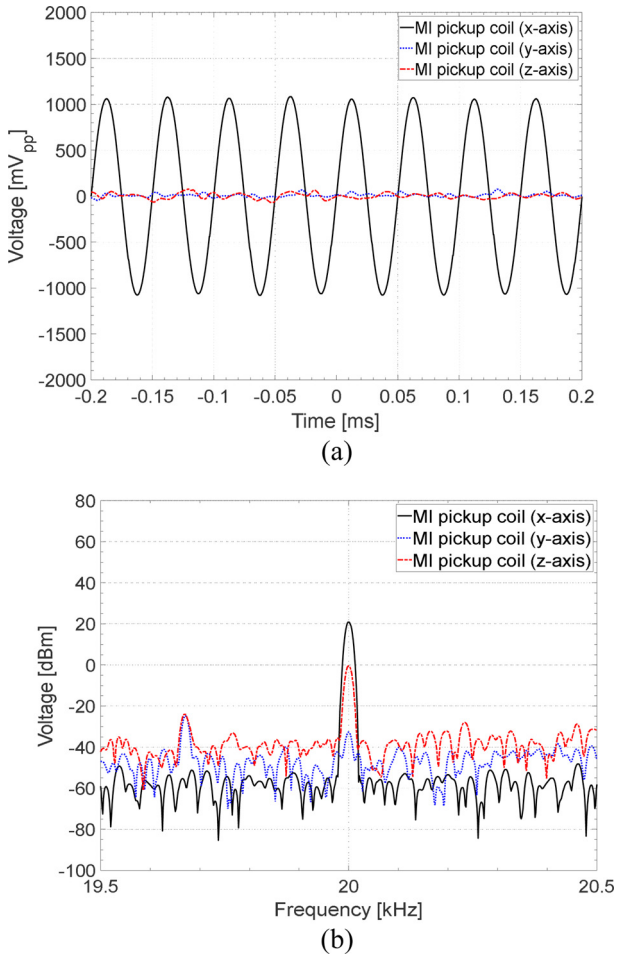

Fig. 3. Output voltage of the three-axis MI sensor at 20 kHz: (a) time-domain. (b) frequency-domain.

where ϕ is the time-varying magnetic flux passing through the pickup coil of the x-axis MI sensor, N is the number of turns of the pickup coil, A is the cross-sectional area of the magnetic material, μ_0 is the permeability constant, and μ_r is the relative permeability of the magnetic material. These parameters increased the output voltage of the sensor, which enhanced the overall performance. However, the improvement effect of these parameters is limited, as increasing them may amplify the thermal and magnetic noise [8]. Therefore, sensor design must consider the optimization of these parameters. Accordingly, the output voltage of the fabricated three-axis MI sensor was measured.

The time-domain output voltage of the three-axis MI sensor measured at 20 kHz for magnetic flux density B_x is shown in Fig. 3 (a). The x-axis MI sensor exhibited the highest output voltage among all three sensors. The output voltage measured from the pickup coil of the x-axis MI sensor was approximately 2.27 V_{pp}. In contrast, the output voltages from the pickup coils of the y- and z-axis MI sensors were approximately 153 and 160 mV_{pp} respectively. These output voltages were significantly lower in amplitude than those of the x-axis MI sensor, with voltage differences of more than 2.05 V_{pp}. Fig. 3 (b) depicts the output voltage measured by the three-axis MI sensor in the frequency domain for magnetic flux density B_x. The output voltage of the x-axis MI sensor was the highest and was measured to be approximately 20.87 dBm at 20 kHz. The output voltages of the y-axis and z-axis MI sensors were approximately -0.49 and -32.07 dBm at 20 kHz, respectively. The output voltage differences relative to the x-axis MI sensor exceeded 20.8 dBm for both y- and z-axis MI sensors. Thus, we confirmed that the x-axis MI sensor of the three-axis MI sensor, aligned with the magnetic flux density B_x applied along the x-axis by the Helmholtz coil, effectively received the signal and exhibited a high output voltage. In contrast, the output voltages of the y- and z-axis MI sensors, which were oriented in different directions, were significantly lower. These results indicated that the proposed three-axis MI sensor exhibits excellent directional signal isolation characteristics and low signal crosstalk. Therefore, the sensor can receive clean signals along the same axis as the transmitter during magnetic field communication, even without prior knowledge of the transmitter orientation.

Fig. 4 shows the measurement results of the three-axis MI sensor used to evaluate the MVCR and linearity, which are key metrics for evaluating sensor performance. As shown in Fig. 4, when the input voltage applied to the Helmholtz coil increased from 0.001 V_{pp} to 10 V_{pp}, the generated magnetic field strength reached a maximum of 1 μT. To evaluate the linearity characteristics of the sensor, we measured the induced voltage (in mV_{rms}) of the three-axis MI sensor (Fig. 4 (a)). The measured induced voltages were 378.5, 376.5, and 377 mV_{rms} for the x-, y-, and z-axis MI sensors, respectively. These results indicated highly linear characteristics of the induced voltage under a magnetic field of up to 1×10^{-6} T. The MVCR (in kV_{rms}/T) of the three-axis MI sensor (Fig. 4 (b)) was calculated from the slope of the induced voltage (Fig. 4 (a)). The measured MVCR values were 378.5, 376.5, and 377 kV_{rms}/T for the x-, y-, and z-axis MI sensors, respectively. In addition, the x-, y-, and z-axis values of the three-axis MI sensor exhibited nearly identical performance in terms of MVCR and linearity.

Fig. 5 shows the evaluation results of the EMNSD for the three-axis MI sensor. The EMNSD, measured across a frequency bandwidth of 18.5–21.5 kHz, determines the weakest detectable magnetic signals in magnetic field communication. The x-, y-, and z-axis MI sensors exhibited EMNSD levels of 0.25, 0.25, and 0.2 pT/√Hz at 20 kHz, respectively. Across the entire measured frequency bandwidth, the three-axis MI sensor maintained consistent noise characteristics, with EMNSD levels remaining below 0.5 pT/√Hz.

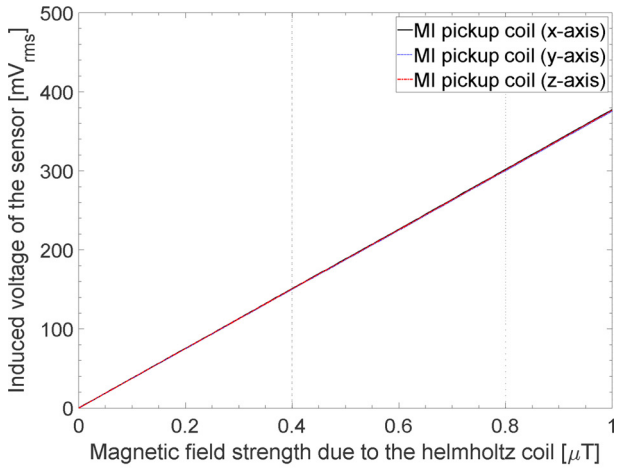

(a)

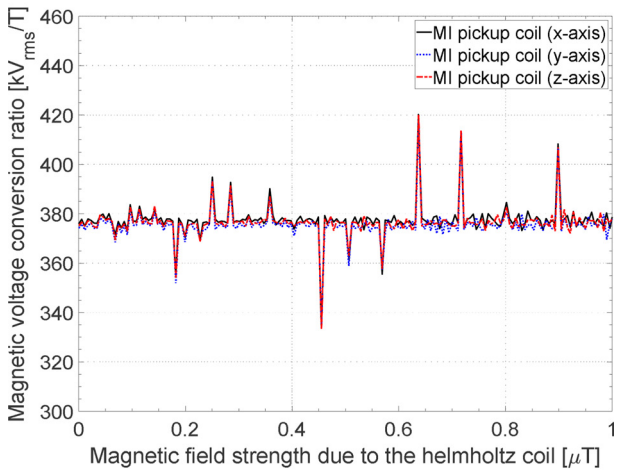

(b)

Fig. 4. Measured results of the induced voltage and magnetic voltage conversion ratio (MVCR) of the three-axis MI sensor: (a) induced voltage at 20 kHz. (b) MVCR at 20 kHz.

Table 2. Comparison with existing MI sensor technology.

Sensor type	MI [8]	MI (This work)
	Pickup coil	Pickup coil
Type (axis)	1	3
Induced voltage (mV$_{rms}$)	267.8	378.5/376.5/377*
MVCR (kV$_{rms}$/T)	268	378.5/376.5/377*
EMNSD (pT/√Hz)	1.68	0.25/0.25/0.2*

*Refers to x-, y-, and z-axis MI sensors of the three-axis MI sensor.

Table 2 summarizes the experimental evaluation results of the three-axis MI sensor and compares them with previously reported MI sensor performance metrics [8]. As indicated, the proposed three-axis MI sensor exhibited superior performance in terms of the linearity of the induced voltage, MVCR, and EMNSD compared with that

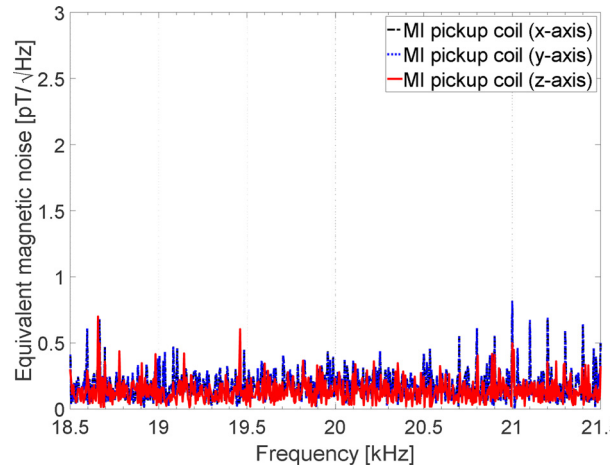

Fig. 5. Equivalent magnetic noise spectral density (EMNSD) of the three-axis MI sensor.

in [8]. These characteristics make it a promising candidate as a receiving element in magnetic field communication systems, particularly in environments where the detection of weak magnetic signals is critical for mid-to-long-range magnetic field communication.

2.3 System Configuration

To verify the feasibility of magnetic-field communication using the proposed three-axis MI sensor, we configured and evaluated a test system in a laboratory setting. The system primarily consisted of a Helmholtz coil as the transmitting antenna, a three-axis MI sensor as the receiving element, an analog-to-digital converter (ADC), and a control PC, as shown in Fig. 6. A carrier frequency of 20 kHz was considered, and the QPSK modulation scheme was employed (Fig. 7 (b)). The modulation signal was generated using an AWG (National Instruments, PXIe-5442) via a graphical user interface (GUI) on a Tx-control PC (PXIe-8861).

via a graphical user interface (GUI) on a Tx-control PC (PXIe-8861).

At the receiving end, the three-axis MI sensor detected an analog QPSK-modulated signal, which was then sent to an ADC (PXIe-5122). Here, the Tx and Rx were controlled using the same PC. The Tx GUI was operated on the transmission side, whereas the RX GUI was operated on the reception side. The Rx PC decoded the modulation signal and output it to a GUI of the Rx PC.

2.4 Results of Magnetic Field Communication Test

Two test scenarios were conducted to evaluate magnetic field communication using the three-axis MI sensor. The first

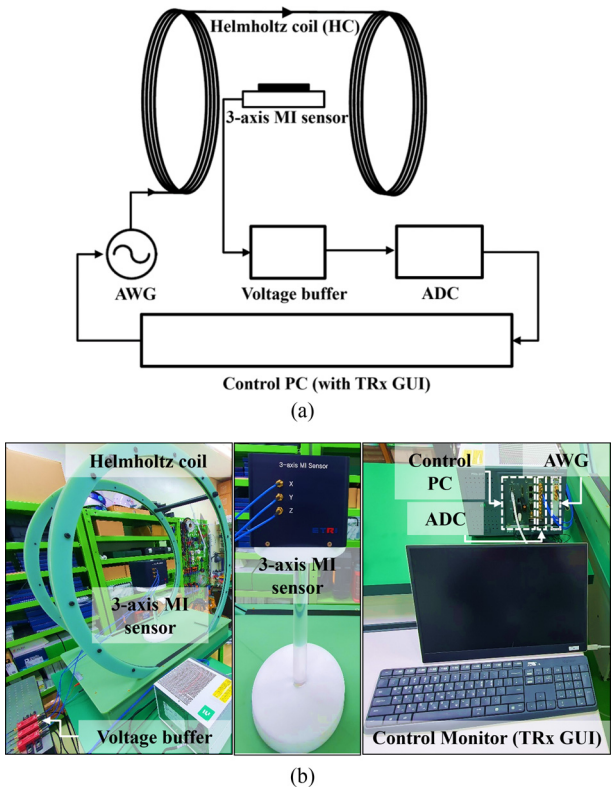

Fig. 6. Magnetic field communication evaluation system: (a) block diagram. (b) experimental setup.

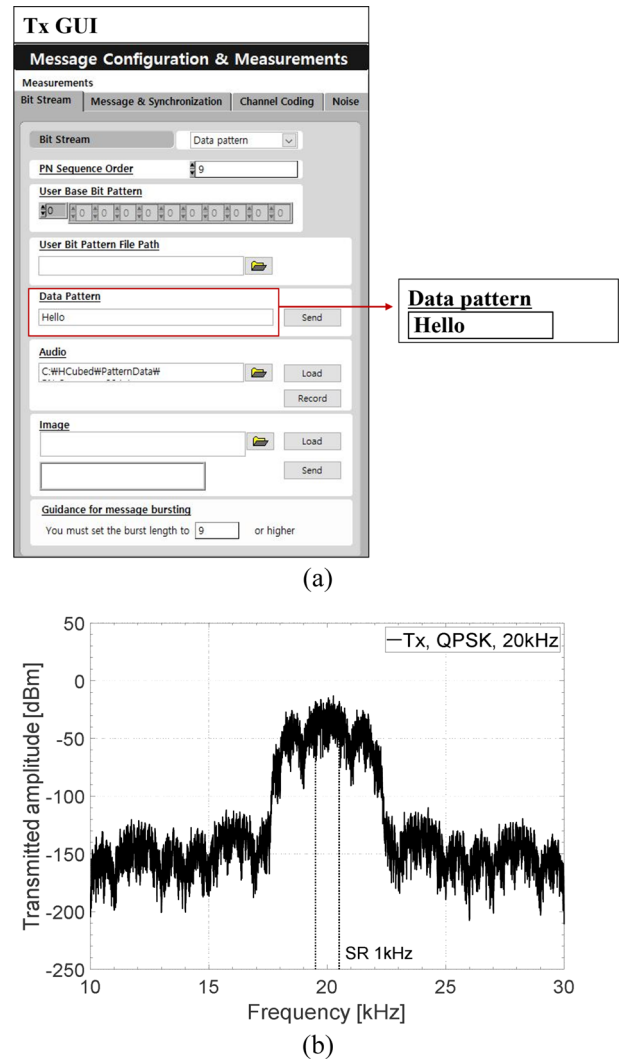

Fig. 7. Modulated transmitted signal of the three-axis MI sensor: (a) the Tx GUI showing the transmitted text data signal. (b) the analog waveform of a QPSK modulated signal with a 1 kHz symbol rate at 20 kHz in the frequency domain.

scenarios focused on evaluating the sensor's ability to demodulate text data. Specifically, the test assessed whether each axis of the three-axis MI sensor, corresponding to the x-, y-, and z-directions, could independently demodulate transmitted text data. In addition, the maximum data rate was evaluated as a function of the symbol rate. The second scenario aims to evaluate the demodulation capability of the sensor for image data signals. In harsh environments where magnetic-field communication is used for emergency purposes, such as during or prior to disaster events, the intuitive transmission of image data may be essential for alert or warning functions. Accordingly, the ability of the three-axis MI sensor to recover the transmitted image data signals was assessed.

To evaluate the first scenario, we used the Tx control PC GUI to set a 20 kHz carrier frequency, 1 kHz symbol rate (corresponding to the bandwidth), and 1 V_{pp} voltage and to transmit the text data signal "Hello" using QPSK modulation. The modulated text data signal was transmitted to the Helmholtz coil via the AWG, and the resulting magnetic field strength was 0.1 μT.

As shown in Fig. 7 (a), the transmitted text data signal "Hello" was displayed on the Tx GUI. Fig. 7 (b) depicts the transmitted analog waveform modulated using the QPSK scheme at a carrier frequency of 20 kHz and symbol rate of 1 kHz.

Fig. 8 shows the demodulation results of the three-axis MI sensor in the first scenario. Fig. 8 (a) shows that the text "Hello" was accurately demodulated and displayed on the RX GUI. Fig. 8 (b) depicts the constellation diagram results, demonstrating that the x-, y-, and z-axis MI sensors independently demodulated the transmitted text data signal. The detailed demodulation results are listed in Table 3. The results confirmed that the x-, y-, and z-axis MI sensors could independently demodulate the text data signal, exhibiting nearly identical demodulation performances.

Fig. 9 shows the results of a magnetic-field communication test conducted to determine the maximum data rate, a key metric derived from the demodulation of transmitted text data signals to evaluate the performance of the three-axis MI sensor as

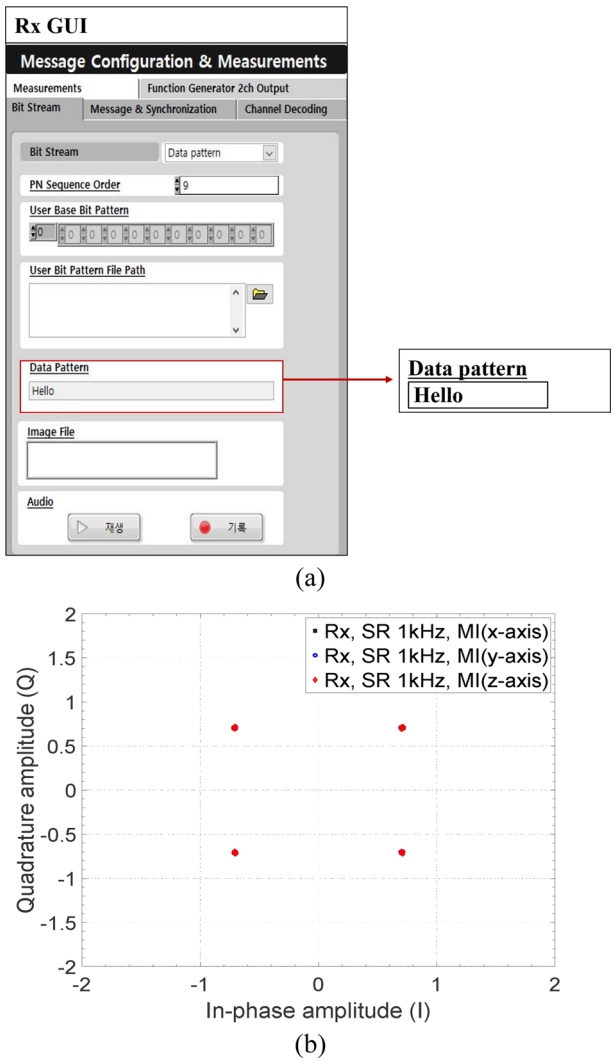

Fig. 8. Demodulation results of the three-axis MI sensor at 20 kHz: (a) Rx GUI displaying the received text data signal. (b) QPSK constellation diagram.

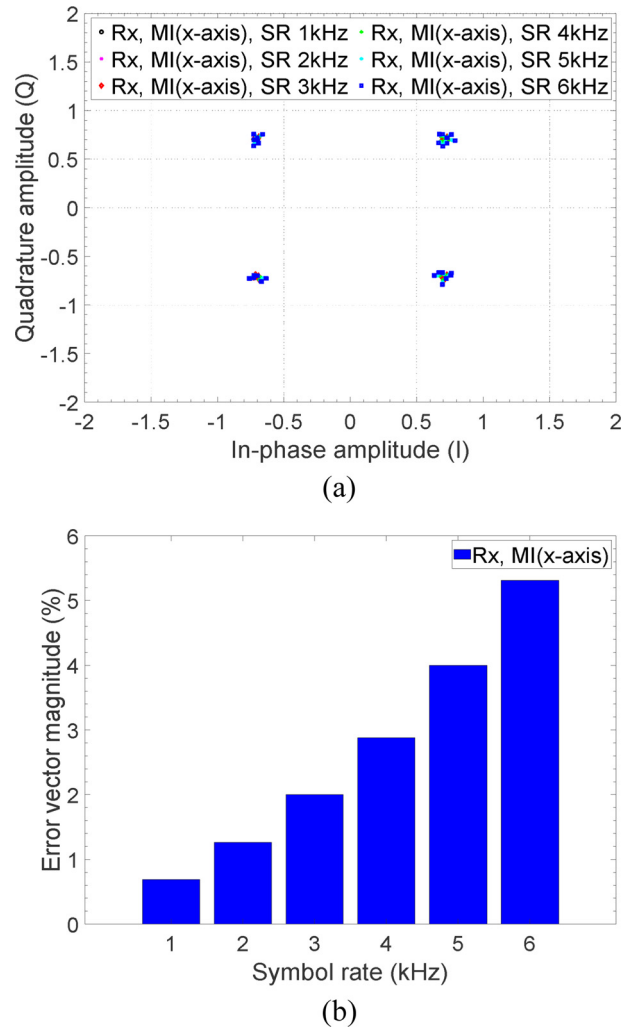

Fig. 9. Communication test results of the x-axis MI sensor of the three-axis MI sensor at 20 kHz, as a function of symbol rate: (a) QPSK constellation. (b) QPSK error vector magnitude.

Table 3. Comparison of demodulation performance metrics for the three-axis MI sensor.

Parameter	Three-axis MI sensor		
	x-axis	y-axis	z-axis
Demodulation	QPSK	QPSK	QPSK
Carrier frequency	20 kHz	20 kHz	20 kHz
Data type	text	text	text
Symbol rate	1 kHz	1 kHz	1 kHz
Data rate	2 kbps	2 kbps	2 kbps
EVM	0.69%	0.69%	0.70%
Estimated E_b/N_0	36.9 dB	36.7 dB	36.8 dB

the receiving element. The Helmholtz coil transmitted the modulated text data signals, and the symbol rate representing the bandwidth was varied as a parameter. The demodulation was performed using the x-axis MI sensor. Fig. 9 (a) shows the constellation results obtained by varying the symbol rate from 1 to 6 kHz. These results confirmed that a maximum data rate of 12 kbps was achieved. Fig. 9 (b) shows the root mean square (RMS) values of the error vector magnitude (EVM) calculated from the constellation results shown in Fig. 9 (a). The RMS value of the EVM was remarkably low at 0.69% for a symbol rate of 1 kHz and increased to 5.9% at 6 kHz. These results are well below the 22.4% threshold defined in the IEEE 802.11ac standard for an acceptable EVM in QPSK. Thus, the three-axis MI sensor successfully received a QPSK-modulated signal with minimal data errors, confirming its high accuracy and reliability. Furthermore, the achieved maximum data rate of 12 kbps is significantly higher than those reported in previous studies [7-10,13,18], indicating the potential of magnetic field communication at voice-level data rates.

Fig. 10 shows the transmitted modulated image signal and corresponding demodulated output obtained from the x-axis MI sensor used to evaluate the second scenario. Fig. 10 (a) shows the Tx GUI for transmitting the "DANGER" image data signal and the frequency-domain analog waveform of the QPSK modulated signal at 20 kHz with a symbol rate of 1 kHz for the image data signal. Fig. 10 (b) shows the demodulation results from the x-axis MI sensor for the transmitted image data signal. The left image in Fig. 10 (b) depicts the "DANGER" image signal successfully demodulated and visualized as an image on the Rx GUI. The right side of Fig. 10 (b) shows the QPSK constellation results at 20 kHz for the demodulated image signal. From the demodulation results shown in Fig. 10 (b), the calculated RMS value of the EVM was 0.54%. Consequently, the image data signal was successfully demodulated. The three-axis MI sensor was confirmed to be capable of demodulating image data signals.

Table 4 shows a comparison of the performance metrics for magnetic field communication. Compared with previously reported magnetic sensor-based communication systems [7,8,10,15,19], the proposed three-axis MI sensor-based system exhibited outstanding performance in terms of transmission data format, data rate, and EVM. These advantages suggest that mid-to-long-range magnetic field communication using the proposed sensor is a promising alternative for operation in harsh environments, such as underwater and underground environments. The results confirm that the three-axis MI sensor is well designed and highly suitable as a receiving element for MI communication applications.

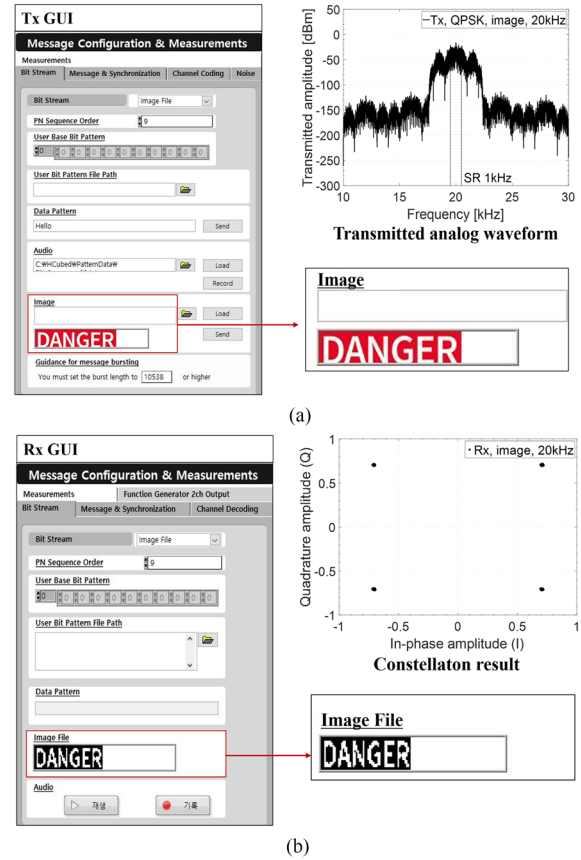

Fig. 10. Modulated transmission and demodulation results for an image data signal: (a) Tx GUI displaying the image data (left) and the QPSK-modulated analog waveform at 20 kHz with a symbol rate of 1 kHz in the frequency domain (right). (b) Rx GUI showing the demodulated image data using the three-axis MI sensor (left) and corresponding QPSK constellation at 20 kHz (right).

Table 4. Comparison of performance metrics for magnetic field communication.

Parameter	Ref. [7]	Ref. [8]	Ref. [10]	Ref. [15]	Ref. [19]	This work
Modulation	QPSK	QPSK	OOK	QPSK	BPSK	QPSK
Carrier frequency	20 kHz	20 kHz	60 kHz	20 kHz	2 kHz	20 kHz
Receiving sensor	RFAM*	DMI	GMI**	DDMI***	Air coil	MI
Sensor axis type	1-axis	1-axis	1-axis	1-axis	3-axis	3-axis
Transmission data format	Binary	Binary	Text	Binary	Text	Text Image
Symbol rate	0.15 kHz	1 kHz	0.1 kHz	1 kHz	0.08 kHz	6 kHz
Data rate	0.3 kbps	2 kbps	0.1 kbps	2 kbps	0.08 kbps	12 kbps (text) 2 kbps (image)
EVM	7.6%	5.60%	-	3.68%	-	5.31% (text) 0.54% (image)
Application	Air	Air	Air	Air	Underground	Air

*RF atomic magnetometer (RFAM)
**Giant magnetoimpedance (GMI)
***Dual differential magnetic induction (DDMI)

3. CONCLUSION

In this paper, a novel three-axis MI sensor is proposed as a receiving element for mid-to-long range wireless magnetic-field communication in harsh environments, including underwater and underground conditions. The proposed sensor enables omnidirectional reception of transmitted signals without requiring prior information on the orientation of the transmitter, thereby effectively overcoming the directional limitations of conventional single- or two-axis MI sensors. In addition, the sensor exhibited excellent magnetic noise performance, achieving levels below approximately 0.5 pT/√Hz within the operating frequency band. These advantages suggest that the proposed sensor is a promising alternative for detecting weak magnetic signals and extending communication distances in extreme environments. The experimental results demonstrate successful QPSK demodulation at 20 kHz in both scenarios. In the first scenario, reliable demodulation of the text data signal was achieved with a maximum data rate of 12 kbps, implying the potential for future voice signal demodulation. In the second scenario, acceptable demodulation performance for the image data signal was confirmed. These results indicate that the proposed three-axis MI sensor can be effectively utilized in MI communication systems for the intuitive transmission of image data in emergencies or disaster situations, serving as a viable solution for alert or warning functions in adverse environments.

CRediT Authorship Contribution Statement

Jang-Yeol Kim: Conceptualization, Methodology, Writing - original draft, Visualization. **In-Kui Cho:** Writing - review & editing, Project administration. **Hyun Joon Lee:** Methodology, Writing - review & editing. **Jung Hoon Oh:** Investigation, Writing - review & editing. **Kye-Seok Yoon:** Conceptualization, Writing – review & editing. **Jae-Ho Lee:** Writing - review and editing, Visualization.

Declaration of Competing Interest

The authors declare that they have no competing financial interests or personal relationships that may have influenced the work reported in this paper.

Acknowledgements

This work was supported by a grant from the Institute of Information & Communications Technology Planning & Evaluation (IITP) funded by the Korean government (MSIT) (No. 2019-0-00007, Magnetic Field Communication Technology Based on 10pT Class Magnetic Field for Middle and Long Range).

REFERENCES

[1] M. Malátek, L. Kraus, Off-diagonal GMI sensor with stress-annealed amorphous ribbon, Sens. Actuators A Phys. 164 (2010) 41–45.
[2] H. Guo, Z. Sun, C. Zhou, Practical design and implementation of metamaterial-enhanced magnetic induction communication, IEEE Access 5 (2017) 17213–17229.
[3] Z. Wang, X. Wang, M. Li, Y. Gao, Z. Hu, T. Nan, et al., Highly sensitive flexible magnetic sensor based on anisotropic magnetoresistance effect, Adv. Mater. 28 (2016) 9370–9377.
[4] N.A. Stutzke, S.E. Russek, D.P. Pappas, M. Tondra, Low-frequency noise measurements on commercial magnetoresistive magnetic field sensors, J. Appl. Phys. 97 (2005) 10Q107.
[5] J.G. Deak, Z. Zhou, W. Shen, Tunneling magnetoresistance sensor with pT level 1/f magnetic noise, AIP Adv. 7 (2017) 056676.
[6] J. Lee, H.J. Lee, J.Y. Kim, I.K. Cho, Gaped two-loop antenna-based magnetic transceiver with an empirical model for wireless underground communication, IEEE Access 9 (2021) 34962–34974.
[7] H.J. Lee, J.H. Oh, J.Y. Kim, I.K. Cho, Performance analysis of atomic magnetometer and bandwidth-extended loop antenna in in resonant phase-modulated magnetic field communication system, ETRI J. 46 (2024) 727–736.
[8] J.Y. Kim, H.J. Lee, J.H. Lee, J.H. Oh, I.K. Cho, Experimental assessment of a magnetic induction-based receiver for magnetic communication, IEEE Access 10 (2022) 110076–110087.
[9] J.Y. Kim, H.J. Lee, J.H. Lee, J.H. Oh, I.K. Cho, Magnetic Induction-Based Test-Bed System for Magnetic Communication in Underground Mines, Proceedings of 20th Annu. IEEE Int. Conf. Sens. Commun. Netw. (SECON), Madrid, Spain, 2023, pp. 388–389.
[10] K. Kim, S. Ryu, J.Y. Kim, I.K. Cho, H.J. Lee, J. Lee, S. Ahn, Giant magnetoimpedance receiver with a double-superheterodyne topology for magnetic communication, IEEE Access 9 (2021) 82903–82908.
[11] Z. Sun, I.F. Akyildiz, Magnetic induction communications for wireless underground sensor networks, IEEE Trans. Antennas Propag. 58 (2010) 2426–2435.
[12] J.H. Ahn, S.H. Lee, T. Lee, Anti-Collision Protocol for Coexistence of RFID and NFC P2P Communications, IEEE Commun. Lett. 20 (2016) 2185–2188.
[13] J.Y. Kim, H.J. Lee, J.H. Oh, K.S. Yoon, J.H. Lee, I.K. Cho, Assessment of a Magnetic Communication Using the Differential Magnetic Receiver in Air/Water Cross-Boundary and Conventional/Non-Conventional Media, J. Magn. 29 (2024) 338–343.
[14] S. Kisseleff, I.F. Akyildiz, W.H. Gerstacker, Survey on advances in magnetic induction-based wireless underground sensor networks, IEEE Internet Things J. 5 (2018) 4843–4856.
[15] J.Y. Kim, H.J. Lee, J.H. Oh, K.S. Yoon, J.H. Lee, I.K. Cho, Dual Differential Magnetic Induction Sensor for Magnetic Communication in Extreme Environments, J. Sens. Sci.

Technol. 33 (2024) 399–405.
[16] M.C. Domingo, Magnetic induction for underwater wireless communication networks, IEEE Trans. Antennas Propag. 60 (2012) 2929–2939.
[17] A. Grosz, E. Paperno, Analytical optimization of low-frequency search coil magnetometers, IEEE Sens. J. 12 (2012) 2719–2723.
[18] J.Y. Kim, H.J. Lee, J.H. Lee, J.H. Oh, I.K. Cho, Experimental results of magnetic communication using the giant magnetoimpedance receiver in underwater environments, J. Electromagn. Eng. Sci. 23 (2023) 533–535.
[19] A. Markham, N. Trigoni, Magneto-inductive networked rescue system (MINERS): Taking sensor networks underground, Proceedings of 11th Int. Conf. Inf. Process. Sensor Netw. (IPSN), Beijing, China, 2012, pp. 317–328.